



Mechanisms of projected sea-level trends and variability in the Southeast Asia region based on MPI-ESM-ER

Yi Jin¹ · Armin Köhl¹ · Johann Jungclaus² · Detlef Stammer¹

Received: 24 February 2023 / Accepted: 9 September 2023 / Published online: 16 September 2023
© Springer-Verlag GmbH Germany, part of Springer Nature 2023

Abstract

The low-lying and densely populated Southeast Asia (SEA) region is threatened by sea-level change. To better understand the mechanism of sea-level change in this region, the sea-level trends and variability in the SEA region are investigated over the historical period 1950–2014 and during 2015–2099 under Shared Socio-economic Pathway5-8.5 scenario forcing, based on the output of the high-resolution ($\sim 0.1^\circ$ for ocean) global climate model MPI-ESM-ER. The results confirm that the SEA steric sea level and its components (i.e., thermosteric, halosteric, and manometric sea level) are rising with accelerations, which are superimposed on El Niño–Southern Oscillation (ENSO) driven variabilities. To understand changes of thermosteric and halosteric sea level, regional-mean ocean heat and freshwater contents are analysed based on physical processes of ocean transports and air-sea fluxes. We show that ENSO variability impacts the thermosteric sea level mainly through lateral ocean heat transports, while it impacts the halosteric sea level mainly through surface freshwater flux. In the projection, a decreased volume transport of the relatively cold water (with respect to the SEA average) from the Pacific warms the SEA region. At the same time, a freshening of the transported saline water (with respect to the SEA average) results in an increased ocean freshwater transport into the SEA region. Locally, the pathway of volume transport from the Pacific to the SEA region is shifting northward, which results in a weakened Indonesian throughflow and an enhanced South China Sea throughflow, both leading to changes of regional sea-level pattern.

Keywords Southeast Asia · Sea Level · Ocean Heat Content · Ocean Freshwater Content · El Niño–Southern Oscillation · Indonesian throughflow

1 Introduction

The Southeast Asia (SEA) region, including the South China Sea (SCS) and the Indonesian Throughflow (ITF), contains the largest archipelago globally and maintains one of the most diverse and active ecosystems in the world. Considering the situation of this low-lying archipelago, there is a great concern regarding future sea-level change as both the ecological diversity and human wellbeing of the SEA are threatened by more frequent flooding and enhanced erosion under climate change conditions (Cazenave and Cozannet 2014; Wetzel et al. 2013). A better quantification of the

projected sea-level change (trend and variability) and an improved understanding of the underlying mechanisms are therefore important for adaptation planning of the coastal communities in the SEA region.

As the only low-latitude passage connecting the Pacific and Indian Ocean, the SEA region plays an important role in the global climate system. For example, the ITF is a key part of the global ocean conveyor belt (e.g., Sun and Thompson 2020), transporting a large volume of warm and fresh Pacific water (approximately 15 Sv ($10^6 \text{ m}^3 \text{ s}^{-1}$); Sprintall et al. 2009; Gordon et al. 2010) into the Indian Ocean. Local circulation changes may influence the SEA ocean heat and freshwater content budgets and further affect sea-level change. Previous studies analyzed the projected ITF changes (e.g., Gupta et al. 2016; Gupta et al. 2021) and variability (e.g., Shilimkar et al. 2022), but seldom mentioned the impact of circulation changes on sea level in the SEA region.

✉ Yi Jin
yi.jin@uni-hamburg.de

¹ Center for Earth System Research and Sustainability (CEN), University of Hamburg, Hamburg, Germany

² Max Planck Institute for Meteorology, Hamburg, Germany

During the altimetry era (1993–2020), the observed linear trend of the SEA sea level rise is $3.8 \pm 1.1 \text{ mm yr}^{-1}$, which is higher than the linear trend of global mean sea level rise of $3.1 \pm 0.4 \text{ mm yr}^{-1}$ over the same period (Ablain et al. 2019), based on the altimetry product from the Archiving, Validation and Interpretation of Satellite Oceanographic (AVISO). However, Strassburg et al. (2015) point out that the SEA sea-level trends based on the two-decade long altimetry data set is dominated by a contribution (roughly 3.5 mm yr^{-1} with spatial differences) from the Pacific Decadal Oscillation (PDO). This highlights that estimates of regional sea-level trends are considerably affected by natural variability. In addition, some studies (e.g., Rong et al. 2007; Liu et al. 2011) find that the sea-level variability in the SCS is highly correlated with the El Niño-Southern Oscillation (ENSO). For basin scale, a large fraction of sea-level variance in the Indo-Pacific region can be explained by combining ENSO, PDO and linear trends simultaneously based on multiple variable linear regression (Zhang and Church 2012; Frankcombe et al. 2015). However, in any case, the physical processes determining how the SEA sea level is influenced by natural variability through ocean transports or surface fluxes are not well understood.

The projected long-term changes of sea level under different emission scenarios have been investigated in previous studies based on global climate models (GCMs) (e.g., Slangen et al. 2014; Zhang et al. 2014; Lyu et al. 2020; Fox-Kemper et al. 2021). However, most of the work focuses on large-scale (basin or globe) patterns, mainly because the adopted low resolution GCMs (typically 100 km or more in the ocean component) are still not adequate for small-scale (e.g., marginal seas) sea level studies, especially for archipelagic regions with complex coastlines and topography like the SEA. Lee et al. (2010) demonstrate that a resolution of 18 km is necessary to resolve the processes of signal propagation through the passages to yield agreement with the intra annual variability of the ITF measurements. Therefore, the projected sea-level trends and its variability in the SEA region have not been fully assessed in a high-resolution model yet.

In this paper, we investigate sea-level trends and variability in the SEA region based on the earth system model MPI-ESM-ER, which features a high-resolution (0.1°) ocean model (Gutjahr et al. 2019), evaluating contributions from the ocean transports and the air-sea fluxes. The remainder of this manuscript is organized as follows. The model and methods are introduced in Sect. 2. In Sect. 3 we first show spatial patterns of projected sea-level change in the SEA and the surrounding oceans, then we focus on the sea-level trends and variability in the SEA region, and its connection to ENSO variability. In Sect. 4 we analyze mechanisms of sea-level trends and variability by investigating

contributions from ocean lateral (ocean transports) and surface (air-sea fluxes) boundaries, respectively. A discussion and final comments follow in Sect. 5.

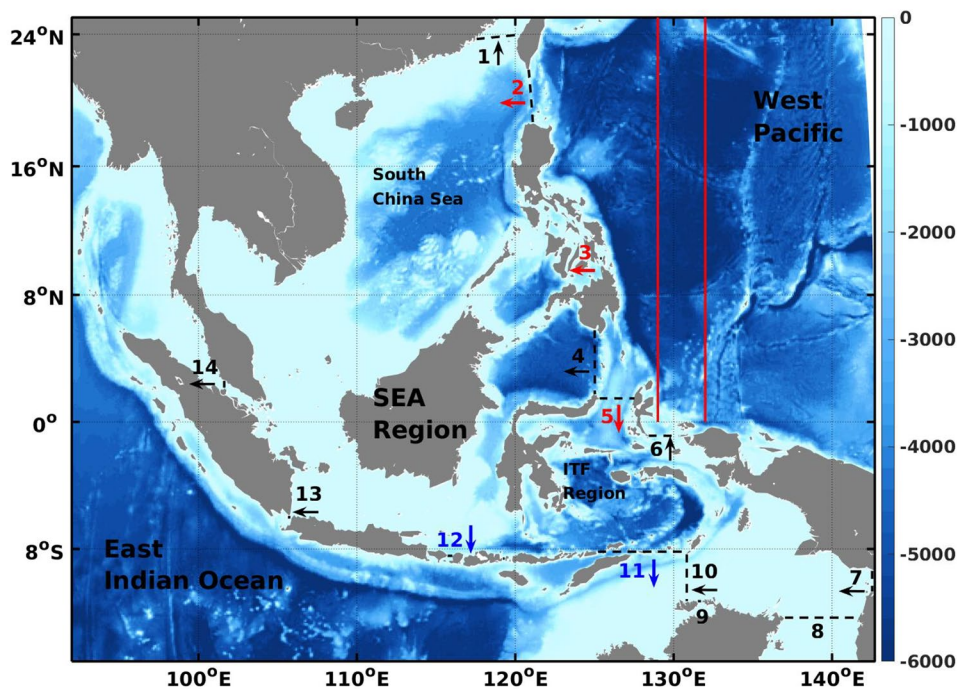
2 Model and method

2.1 MPI-ESM-ER and the study domain

The data used in this paper are obtained from the simulations of the Max Planck Institute for Meteorology Earth System Model 1.2 (MPI-ESM1.2; Mauritsen et al. 2019), which couples the atmosphere, ocean and land modules through exchange of energy, momentum, water and carbon dioxide. MPI-ESM1.2 is available in several configurations with different resolutions of atmosphere and ocean models and different complexity of integrated processes. MPI-ESM1.2 simulations contributed to the sixth phase of the Coupled Model Intercomparison Project (CMIP6) (e.g., Wieners et al. 2019 for MPI-ESM-LR; Müller 2018 for MPI-ESM-HR; Gutjahr et al. 2019 for MPI-ESM-ER), among which MPI-ESM-ER is the model with the finest resolution in the ocean (about 6–11 km) and approximately 100 km for the atmosphere. At this resolution in the ocean model, eddies are resolved over large parts of the ocean, hence it is named as ER (eddy-rich). Wickramage et al. (2023) present the sensitivity of sea-level projections to ocean spatial resolution based on MPI-ESM-LR, HR and ER results, indicating the MPI-ESM-ER produced more reliable sea-level changes especially in the eddy active regions like the western Pacific.

Following the High-Resolution Model Intercomparison Project protocol (Haarsma et al. 2016), the historical simulation of MPI-ESM-ER covers 1950 to 2014, while the projection runs from 2015 to 2099 (called future period hereafter) under the Shared Socio-economic Pathway (SSP) 5-8.5 (more details in Gutjahr et al. 2019). To keep the consistency in presenting the changes from the historical period to the future, the combined period 1950 to 2099 is analyzed together in this work. Our study domain (92°E – 142°E , 15°S – 24°N) is centered on the SEA region, including parts of the western Pacific and the eastern Indian Ocean (Fig. 1). The SEA region is defined as the area enclosed by 14 straits/channels (hereafter all called straits) (Fig. 1) with their specific longitudes and latitudes listed in the supplemental material (Table S1). The SEA region roughly can be subdivided by the Borneo Island into the SCS and the ITF regions. The change of ITF transport could be roughly estimated by the volume transport changes through Straits No. 4–5 (ITF inflow from the Pacific) and Straits No. 11–12 (ITF outflow to the Indian Ocean), which account for most of the ITF transport (Sprintall et al. 2009).

Fig. 1 Southeast Asia (SEA) study region and its bathymetry (m). The SEA region is enclosed by 14 straits/channels indicated by dashed lines and numbers. The arrows near the strait numbers indicate the directions of the long-term averaged volume transports (1950–2014). As the volume transports through Straits No. 8 and 9 are much weaker than the others, their directions are not presented. The straits indicated by red (blue) numbers and arrows are the most important inflows (outflows), which are discussed in Sect. 4.3. The westward velocity averaged between the two red lines are used to measure the meridional variation of the volume transport from the Pacific to the SEA region (Sect. 4.4)



2.2 Model de-drifting and estimation

Considering the long-term simulations could be contaminated by model drift owing to a disequilibrium ocean state, we subtract the drift from the historical and scenario simulations, which is obtained from the control simulation carried out with fixed forcing of the 1950s climatology (Gutjahr et al. 2019). Different variables can show different drift behavior (Gupta et al. 2013). Therefore, linear regression is applied for dynamic sea level (DSL) and global mean thermosteric sea level (TSSL) de-drifting, while quadratic regression is applied for ocean temperature and salinity de-drifting before obtaining regional steric sea level.

After de-drifting, the historical sea-level variability of the MPI-ESM-ER simulation in the study region is evaluated against the altimeter product AVISO for the period of 1993–2020. An Empirical Orthogonal Functions (EOF) analysis is applied to the AVISO sea level anomaly (SLA) and MPI-ESM-ER DSL after removing their own global means and seasonal cycles (results in the supplemental material Fig. S1). The spatial patterns of their first modes are very similar (pattern correlation of 0.84; pattern root mean square deviation of 0.03 m) with a strong signal in the western Pacific. Both principal components of the first modes (PC1) show high correlations with the corresponding Niño 3.4 indexes (0.69 between AVISO SLA and Niño 3.4 index from Hadley Centre Sea Ice and Sea Surface Temperature data set (Rayner et al. 2003); 0.86 between MPI-ESM-ER DSL and its Niño 3.4 index), which is used to represent the ENSO variability (Trenberth 1997). The Niño 3.4 index is defined

as sea surface temperature (SST) anomalies within [5°N–5°S, 170°W–120°W] after removing the global mean SST. This result illustrates that the MPI-ESM-ER simulates sea-level variability in the study region well by representing realistic spatial pattern and by capturing natural variability.

To estimate the capability of the strait transport simulation within the SEA region in MPI-ESM-ER, the simulated transports are compared with the observed ITF transports from the International Nusantara Stratification and Transport (INSTANT) program (Gordon et al. 2010). The comparison within the five straits (listed in the supplemental material Table S2) shows that the model underestimates the ITF (11-Sv simulated result with respect to the 15-Sv observed total ITF transport; Gordon et al. 2010).

2.3 Ocean heat and freshwater transports computation

To understand sea-level changes caused by ocean temperature and salinity anomalies, ocean heat and freshwater transports through SEA straits are involved during the analysis. The calculation of ocean heat transport (OHT) through a section with depth H adopts a modified scheme following Lee et al. (2004) by involving the time-dependent volume-averaged temperature of the SEA region T_{mean} ,

$$OHT = \rho c_p \iint_0^H V \bullet (T - T_{mean}) dz dx, \tag{1}$$

in which ρc_p is the volumetric heat capacity ($4 \cdot 10^6 \text{ J K}^{-1} \text{ m}^{-3}$ in MPI-ESM-ER), V is the velocity normal to a cross section, T is the temperature at the section, dz and dx indicate integrating along the depth and width of the section, respectively. By including the temperature anomaly ($T - T_{mean}$), this OHT identifies the relative heat contribution to the study domain. This modified scheme has been widely applied in ocean heat content (OHC) budget studies (e.g., Zhang and McPhaden 2010; Thompson et al. 2016).

The ocean freshwater transport (FWT) used in ocean freshwater content (FWC) budget was defined in previous FWC studies as,

$$FWT = \iint_0^H V \cdot \frac{S_{ref} - S}{S_{ref}} dz dx, \quad (2)$$

(e.g., Rabe et al. 2011; Köhl and Serra 2014), in which S is the salinity at the section, and S_{ref} is the reference salinity. Here, we adjust this definition following the same strategy as the modified OHT definition, yielding

$$FWT = \iint_0^H V \cdot \frac{S_{mean} - S}{S_{ref}} dz dx, \quad (3)$$

where S_{mean} is the time-dependent volume-averaged salinity of the SEA region, and S_{ref} is defined as the long-term mean (1950–2099) of S_{mean} (a constant of 34.5 psu). The modified FWT (Eq. 3) distinguishes whether individual transports contribute to freshening or salinification of the SEA region, based on the salinity difference from the regional mean ($S_{mean} - S$).

Hereafter, all the OHT (FWT) are estimated relative to the regional mean temperature (salinity) of the SEA region following Eq. 1 (Eq. 3). Specifically, positive OHT (FWT) means heating (freshening) the SEA, while negative OHT (FWT) cools (salinizes) the SEA region. Similarly, positive (negative) volume transport indicates increasing (decreasing) water volume in the SEA region.

Both the OHT and FWT integrated within the depth range H can be decomposed into the contributions from time-mean ocean properties (temperature or salinity) \bar{f} , time-mean velocity \bar{v} , and their respective anomalies f' and v' (Köhl and Serra 2014),

$$F_{t/w} = \iint_0^H f v dz dx = \iint_0^H \left(\bar{f} \bar{v} + \bar{f} v' + f' \bar{v} + f' v' \right) dz dx, \quad (4)$$

where $F_{t/w}$ denotes the OHT or FWT. Since the product of the two time-independent values $\bar{f} \bar{v}$ is a constant, and the product of the two anomalies $f' v'$ is found to contribute little to the total flux $F_{t/w}$, only the changes due to the changes of temperature (or freshwater) $f' \bar{v}$ and velocity

$\bar{f} v'$ are presented and compared with the total transport during analysis (Sect. 4). To present the projected changes relative to the historical period, the anomaly (v' and f') are defined with respect to the historical mean (1950–2014).

3 Sea-level trends and variability in the SEA region

Firstly, to provide the basic knowledge of sea-level change in the study domain, the spatial patterns of projected sea-level change in the SEA region and its surrounding oceans are presented (Fig. 2). The differences between the averages of the last two decades during the future (2080–2099) and historical (1995–2014) periods are used to present the projected regional sea-level changes. The sum of regional DSL (relative to global mean) and global mean TSSL is steric sea level (SDSL; Gregory et al. 2019), which can be decomposed into regional TSSL, halosteric sea level (HSSL), and manometric sea level (MMSL) (Gregory et al. 2019):

$$\begin{aligned} \text{Regional SDSL} &= \text{Regional DSL} + \text{Global mean TSSL} \\ &= \text{Regional TSSL} + \text{Regional HSSL} + \text{Regional MMSL}. \end{aligned} \quad (5)$$

The DSL changes are closely related to upper ocean current changes through the geostrophic balance. In the western Pacific and around the Luzon Strait (Strait No.2 in Fig. 1), the DSL increases on the northern side and decreases on the southern side (Fig. 2a), indicating larger volume intrusion into the SCS, and an anti-clockwise circulation anomaly, which is also reflected in the DSL changes in the SCS (low sea-level center). These DSL and current changes are consistent with a previous dynamical downscaling study based on CMIP5 models (Jin et al. 2021). For the Indian Ocean part, there is a negative sea-level center west of the Sumatra Island (north of Strait No.13 in Fig. 1) showing the increasing outflow through the Sunda Strait (Strait No.13) from the SEA region to the Indian Ocean.

The TSSL change is positive over the entire study domain, with larger change in the Indian Ocean than that in the Pacific (Fig. 2b). However, the HSSL change has opposite signs in the Pacific and Indian Ocean (Fig. 2c). These changes of TSSL and HSSL are connected to regional ocean heat and freshwater content changes, which are modulated by ocean transport and air-sea flux together (further discussed in Sect. 4). Considering the regional mean over the study domain, the TSSL change (12.2 cm) is the main contributor to the SDSL change (20.0 cm), much larger than the contribution from the HSSL (2.5 cm). On the other hand, the TSSL change in the study domain (12.2 cm) is smaller than the global mean TSSL change (20.3 cm), which is caused

by the broad shallow continental shelves in the SEA region. The MMSL change (also called mass sea level component and equivalent to ocean bottom pressure; e.g., Wu et al. 2017) is associated with ocean mass redistribution. The pattern of MMSL change almost reflects the pattern of bathymetry (pattern correlation of -0.82), showing more water flows into the continental shelves from open ocean leading to 5.3 cm regional mean sea level rise (Fig. 2d). With the same density anomaly, the deep region shows larger steric sea level anomaly (namely water volume change caused by density variation) compared with that in the shallow region, and the larger steric anomaly is spread over the entire ocean surface leading to positive bottom pressure change on the continental shelves (Landerer et al. 2007).

To illustrate how ocean model resolution affects sea-level projections in the SEA region, the results from MPI-ESM-LR are also presented as a comparison (Fig. 2e-h), whose ocean resolution is roughly 150 km. DSL changes in MPI-ESM-LR share similar spatial patterns and the same regional mean with MPI-ESM-ER, but with weaker sea-level gradient (Fig. 2e). MPI-ESM-LR presents 3.2 cm larger regional-mean TSSL change than that in MPI-ESM-ER, mainly induced by more significant thermal expansion in the western Pacific and eastern Indian Ocean (Fig. 2f). Since the salinization in the eastern Indian Ocean is missing in MPI-ESM-LR, its HSSL change is larger than that in MPI-ESM-ER (with regional mean change of 1.5 cm; Fig. 2g). However, different from TSSL and HSSL changes, the MMSL in MPI-ESM-LR shows smaller change (with regional mean change of 1.3 cm) than that in MPI-ESM-ER. As MMSL change signals cover mostly shallow regions, the

difference is caused by the missing ocean points in MPI-ESM-LR (Fig. 2h).

After presenting the spatial patterns of sea-level change in the study domain, we further extract the dominant spatiotemporal information of sea-level change. Therefore, an EOF analysis is also applied for the SDSL after removing the seasonal cycle during the whole historical and future periods (1950–2099). Recalling that the western Pacific is deeply affected by natural variability like ENSO (as demonstrated by the evaluation result above; Fig. S1), the EOF analysis is applied specifically for the SEA region to eliminate any influence from the Pacific and Indian Ocean on the analysis. The resulting EOF first mode (EOF1) shows spatially coherent sea-level changes with the strongest signals in shallow regions (Fig. 3a). Since the global mean thermal expansion is included in the SDSL, the PC1 reveals an accelerated trend over 1950–2099 (Fig. 3b). After removing the linear-plus-quadratic fit of the PC1, the residual PC1 of the SDSL matches well with the Niño 3.4 index (correlation 0.71; Fig. 3b). Therefore, EOF1 illustrates an accelerating rise of the SDSL over the whole SEA region superimposed on ENSO driven fluctuations.

EOF analyses are also applied to the individual SDSL components (i.e., TSSL, HSSL, and MMSL) after removing the seasonal cycles. The EOF1 of TSSL (Fig. 3c) also shows a region-coherent mode with the strongest signal in the ITF region, the second strongest in the SCS basin, and the weakest on the continental shelves. This non-uniform pattern is mainly caused by the differences in the local bathymetry (pattern correlation of 0.81 between Figs. 1 and 3c). The PC1 time series indicate an accelerating trend of TSSL over 1950–2099 under global warming (Fig. 3d). Similar to the

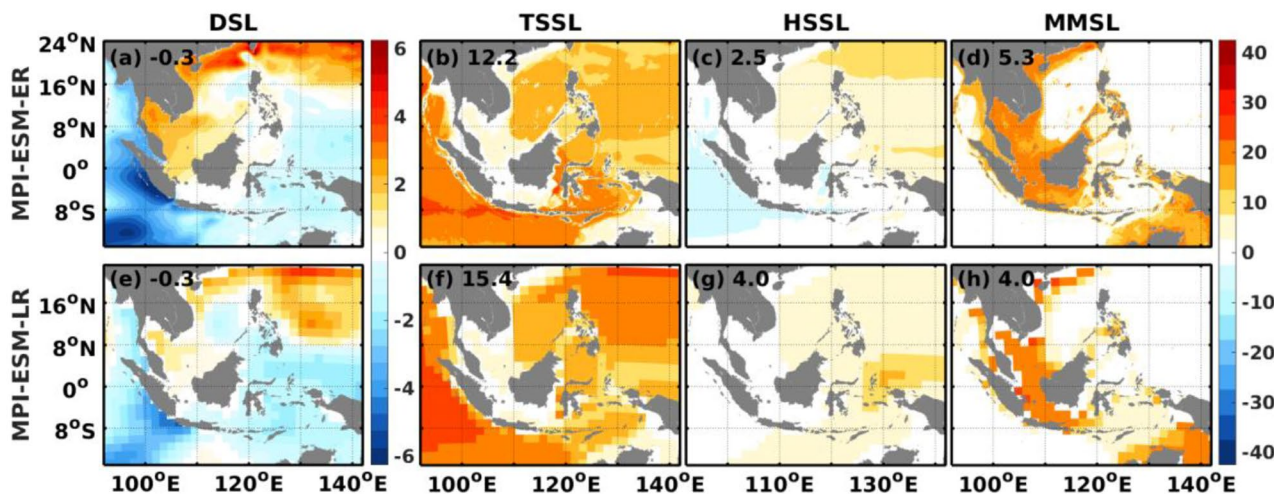


Fig. 2 Projected changes of (a) Dynamic Sea Level (DSL; cm; relative to global mean), (b) thermosteric sea level (TSSL; cm), (c) halosteric sea level (HSSL; cm), and (d) manometric sea level (MMSL; cm) between two mean states of 2080–2099 and 1995–2014 based on MPI-ESM-ER results. (e)–(h) are the same as (a)–(d) but based on

MPI-ESM-LR results. Numbers in the upper-left corners of each panel represent regional averages (cm), with the global mean TSSL changes of 20.3 cm in MPI-ESM-ER and 23.6 cm in MPI-ESM-LR. All the changes are presented in their original resolutions (roughly 10 km for MPI-ESM-ER and 150 km for MPI-ESM-LR).

EOF result of SDSL, after removing the linear-plus-quadratic fit of the PC1 time series, the residual PC1 of TSSL also reveals connection to the Niño 3.4 index (correlation of 0.64). Therefore, the first mode of the SEA TSSL expresses an accelerating warming superimposed on fluctuations related to ENSO. A similar result is also found in the EOF result of HSSL (Fig. 3f; correlation of 0.61 after detrending). However, the magnitude of EOF1 of HSSL is smaller than that of TSSL (all the PCs are normalized). There are stronger SSH signals in the SCS basin, which is the shallower region, compared with the ITF region (Fig. 3e). This indicates that the ocean freshening in the SCS basin is more pronounced than that in the ITF region, outweighing the effect from bathymetry, which can be confirmed by the regional depth-averaged ocean salinity change from the historical to future periods (not shown). The EOF analysis of MMSL indicates that more water mass is transferred to the SEA continental shelves from the deep region, showing opposite pattern against the EOF1 of TSSL (pattern correlation -0.94 ; Fig. 3 g and c). The MMSL is in response to ocean water redistribution caused by ocean dynamics which is also related to ocean temperature and salinity anomalies.

Therefore, the MMSL also shows variability under the influence of ENSO (correlation of 0.73 between detrended PC1 and Niño 3.4 index) with accelerating trend (Fig. 3h).

The EOF results demonstrate that both the forced long-term trend and ENSO-related variability of sea level share the same spatial patterns (Fig. 3a, c, e and g), which all show the feature of topography. For the sea-level change under long-term forcing, its connection to bathymetry is discussed above (Fig. 2). While for the ENSO-related variability of sea level, we suppose that deep region, compared with shallow region, provides a larger container to hold heat and freshwater, and it absorbs (or releases) larger heat content (or freshwater content) under the same intensity of influence from ENSO.

4 Causes of sea-level trends and variability

4.1 Regional-mean ocean heat and freshwater content budgets

Since TSSL and HSSL changes were defined based on vertical-integrated temperature and salinity anomalies, which

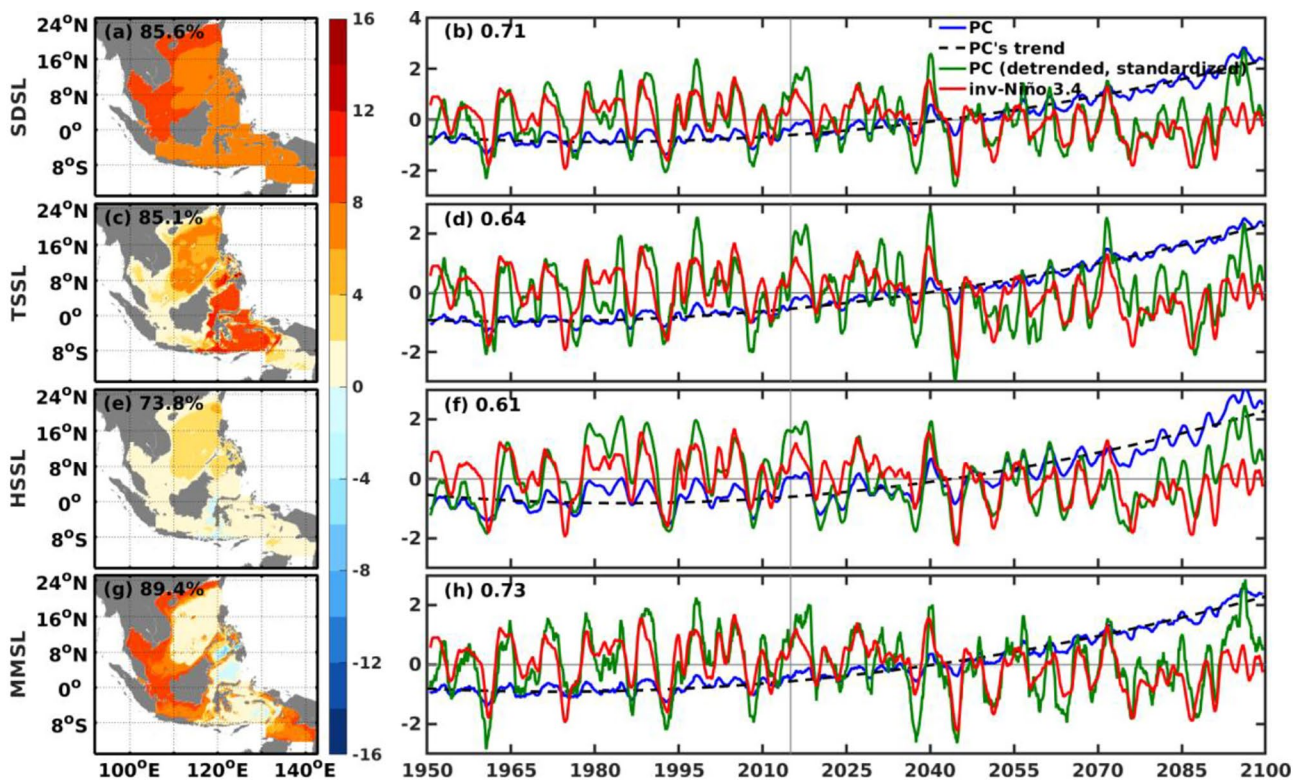


Fig. 3 Spatial patterns of the first mode Empirical Orthogonal Function (EOF) of (a) SDSL (cm), (c) TSSL (cm), (e) HSSL (cm), and (g) MMSL (cm) over the period 1950–2099. Explained variances are given in the upper-left corners of each panel. The corresponding principal components (PCs; blue; 13-month running mean) are shown in panels in (b), (d), (f), and (h), superimposed to the inverse Niño 3.4 index (red; 13-month running mean). The black dashed lines in (d), (f),

and (h) are the quadratic least-square fitted curves of the corresponding PCs showing the trends of the PCs, and the green lines indicate the detrended and standardized PCs. The correlation coefficients between the inverse Niño 3.4 index and the detrended PCs of SDSL, TSSL, HSSL and MMSL are 0.71, 0.64, 0.61, and 0.73, respectively. Historical and future periods are separated by vertical grey lines in 2015

are closely related to OHC and FWC changes, in this section the contributions to regional-mean TSSL and HSSL are discussed in terms of heat and freshwater fluxes/transport from atmosphere and ocean, respectively.

Before discussing the individual contributions from atmosphere and ocean, the regional-mean OHC and FWC budgets are estimated in the SEA region. In the climatological balance, the total surface heat flux (SHF) and surface freshwater flux (SFF) from atmosphere always heat the SEA region and make the ocean fresher, respectively, while the transports through the ocean straits cool off the SEA region and make the ocean water saltier (Fig. 4). The sum of fluxes and transports from all boundaries (i.e., ocean surface and lateral boundaries of the SEA region) is roughly equal to the changes of OHC and FWC (obtained based on integrated the interior ocean temperature and salinity), which demonstrates that the budgets can generally be closed, indicated by two orders of magnitude smaller residuals (Fig. 4). The residuals could result from using monthly averaged model output, as there is no available snapshot output. The missing diffusion and sub-monthly eddy flux terms in the estimation could also contribute to the residual time series. The correlation coefficient between Niño 3.4 index and regional mean OHC (FWC) is -0.61 (-0.66) after detrending, which

indicates smaller OHC (FWC) during the El Niño periods and larger OHC (FWC) during the La Niña periods.

For the OHC budget, the lead-lag analysis indicates that the time series of OHT leads SHF by 6 months with a correlation of -0.81, which suggests that SHF responds passively to OHC variations resulting from OHT variations. In other words, the atmosphere is damping OHC anomalies through the interaction with SST. This is the reason why the standard deviation of SHF and SHF + OHT are both smaller than that of OHT (Fig. 4a). In contrast, for the FWC budget, the time series of FWT lags SFF 19-month with correlation of -0.91, showing that FWC changes are primarily driven by SFF, and subsequent divergence of the FWT. In summary, the OHC variability is mainly caused by ocean transports, while the FWC variability is mainly induced by air-sea fluxes.

The long-term means of atmosphere fluxes and ocean transports during the historical and future periods and their differences are also shown (Fig. 4b and d). For the time-mean states in the historical period (1950–2014), there are quasi-stationary balances between atmosphere fluxes and ocean transports for both heat and freshwater. It indicates stable states of the regional-mean OHC and FWC. In the future period (2015–2099), the enhanced warming effect of SHF is more significant than the enhanced cooling effect of OHT, which breaks the balance in the historical period and

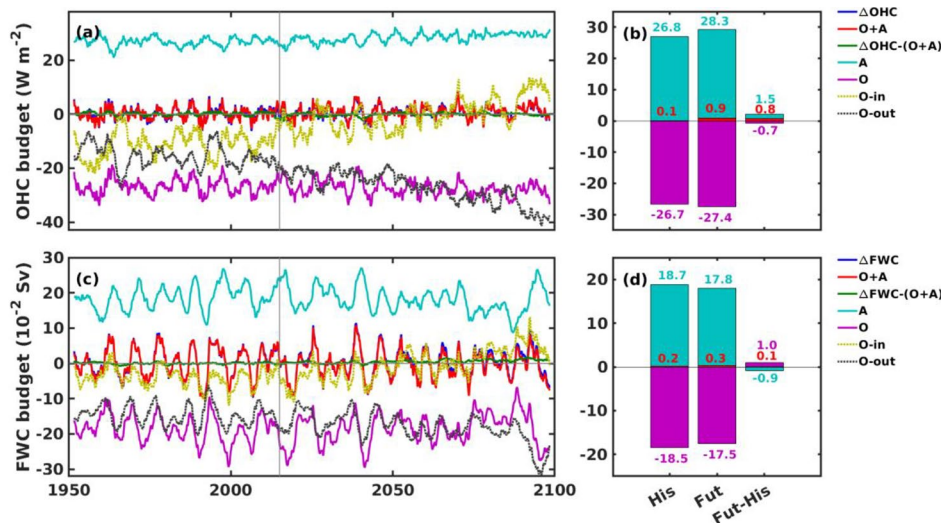


Fig. 4 (a) Time series of components contributing to the ocean heat content (OHC) budget (units $W m^{-2}$), displayed as the surface heat flux (“A” in legend; teal) and ocean heat transport convergence (“O” in legend; purple); the sum of fluxes through 14 straits in Fig. 1). Positive values correspond to heating of the ocean. The sum of the contributions from atmosphere and ocean (“O+A” in legend; red), the changes of OHC (“ Δ OHC” in legend; blue), and their differences (“ Δ OHC-(O+A)” in legend; green) are also shown. The contribution by ocean transports (purple) is further separated into the inflow from the Pacific (“O-in” in legend; the sum of transports through Straits No.1–7 in Fig. 1; dashed yellow line) and outflow to the Indian Ocean (“O-out” in legend; the sum of transports through Straits No.8–14 in Fig. 1; dashed black line). All the ocean heat transports are divided by

the SEA area to yield $W m^{-2}$. (b) Graphs of the contributions from atmosphere (teal), ocean (purple) and their sums (red) with values attached (the same unit as (a)), which are averaged during historical period (“His”; 1950–2014), future period (“Fut”; 2015–2099) and their changes (“Fut-His”) from left to right. (c) and (d) are the same as (a) and (b) but for ocean freshwater content (FWC; its change is indicated as “ Δ FWC” in legend) budget (units 10^{-2} Sverdrup; Sv), and positive value means freshening the ocean. All the time series in (a) and (c) are filtered by a 37-month running mean. The standard deviation is $2.21 W m^{-2}$ ($0.04 Sv$) for heat (freshwater) fluxes from all boundaries, $2.24 W m^{-2}$ ($0.04 Sv$) for the change of OHC (FWC), and reduced to $0.63 W m^{-2}$ ($0.00 Sv$) for the residuals

results in accelerating OHC changes in the future. However, both SFF and FWT were weakened in the future with similar magnitudes, which means SFF and FWT provide roughly equivalent contributions to FWC change. The positive sums of fluxes and transports (0.9 W m^{-2} in Fig. 4b, $3 \times 10^{-2} \text{ Sv}$ in Fig. 4d) accumulating with time during the future period lead to upward trends of TSSL (Fig. 3d) and HSSL (Fig. 3d), respectively.

The ocean heat and freshwater transports through the SEA ocean boundaries are further separated into the eastern (Straits No.1–7 in Fig. 1) and western (Straits No.8–14 in Fig. 1) parts, based on the basic current pattern of inflow from the Pacific and outflow to the Indian Ocean (long-term mean current directions shown in Fig. 1 by arrows). Both the inflow and outflow cool and salinize the SEA during the historical period without obvious trend (Fig. 4). However, the inflow turns to heat and freshen the SEA region under climate change roughly after 2070. The positive trends in the inflows during the future period are reflected by similar negative trends in the outflows (Fig. 4). These transport changes from the historical to future periods are further analyzed in the following sections.

Compared with the projected changes of total OHT and FWT, there are more obvious linear trends shown in inflow and outflow transports. Specifically, the change of outflow OHT cooling effect (-10.9 W m^{-2} between historical and future means) is larger than that of inflow OHT (10.2 W m^{-2}); however, the change of inflow FWT ($4.0 \times 10^{-2} \text{ Sv}$) shows larger impact than the outflow ($-3.0 \times 10^{-2} \text{ Sv}$) in the FWC budget. This difference indicates that velocity is not the dominated element, at least not the only one, that impacts the trends of both OHT and FWT. The contribution from temperature or salinity change is not negligible which is also proved by the transport decomposition results below.

4.2 Individual contributions from air-sea fluxes and ocean transports

4.2.1 Air-sea heat and freshwater fluxes

For the contributions from the atmosphere, the spatial pattern of time-mean SHF from the historical to future periods presents positive changes (warming effect) in almost all of the SEA region (Fig. 5a), while the positive change (freshening effect) of SFF mainly concentrates on the south part of the SCS (Fig. 5b). However, these mean-state changes are both quite small compared with their corresponding variability, which can be proven by combining the EOF results (regional mean is not removed). The EOF1 of SHF shows the SEA region is warmed and cooled together under the effect of ENSO (correlation between PC1 and Niño 3.4 index is 0.76) with a high-amplitude center located around

the Taiwan Island (Fig. 5c and e). Similarly, the EOF1 of SFF in this region is dominated by the ENSO variability as well (correlation between PC1 and Niño 3.4 is 0.79; Fig. 5d and e). Furthermore, the regional mean SFF shows correlation of 0.66 with FWC (after detrending). This demonstrates that SFF is an important factor that transmits the large-scale ENSO variability to the local FWC in the SEA region, which further influences the local HSSL variability. However, the negative correlation of -0.62 between regional mean SHF and OHC (after detrending) illustrates that SHF is damping OHC anomalies, and this also supports the conclusions drawn in the last section.

4.2.2 Ocean heat and freshwater transports connecting the Pacific and Indian Ocean

For the contributions from the oceanic processes, both the variabilities of the inflows from the Pacific and outflows to the Indian Ocean (dashed lines in Fig. 4a and b) are decomposed into the contributions from velocity change v' and ocean properties (temperature and salinity) change f' based on Eq. 3 (Fig. 6). The total inflow OHT from the Pacific is stable during the historical period and increases considerably during the future period with fluctuations superimposed (Fig. 6a). Based on this comparison, both the trend and variability of the inflow OHT ($\int_0^H f v dz dx$) are mainly induced by the contribution from velocity change ($\int_0^H \bar{f} v' dz dx$), indicated by time-mean changes and high correlation (0.97) (Fig. 6a). While, the contribution from temperature change ($\int_0^H f' \bar{v} dz dx$) presents much smaller standard deviation with a weaker trend. However, the sign of velocity trend, namely increasing or decreasing volume transport, could be different from the trend of the velocity contribution ($\int_0^H \bar{f} v' dz dx$), which is weighted by temperature anomalies. Hence, the time series of velocity change (namely volume transport change)

$$F_v = \int_0^H v' dz dx, \quad (6)$$

is presented as a reference (thin black lines in Fig. 6), which is also relative to the SEA region (positive means more water in the SEA). Combined with the time series of the velocity change, it is confirmed that the increasing trend and variability of the OHT from the Pacific to the SEA region is caused by the decreasing volume transport and the variability of volume transport, respectively. A similar situation is also found for the outflow OHT. The outflow OHT is affected by the inflow OHT, indicated by the correlation of -0.92 with 6-month lag (blue lines in Fig. 6a and c). The outflow OHT results in decreasing OHC in the SEA region mainly caused by the reduced volume transport (Fig. 6c).

Fig. 5 The spatial patterns of (a) surface net downward heat flux changes ($W m^{-2}$) and (b) surface net freshwater flux into the ocean ($10^{-8} m s^{-1}$) between historical mean (1950–2014) and future mean (2015–2099) with the regional means shown in the upper-left corners. The first EOF of (c) surface net downward heat flux ($W m^{-2}$), and (d) surface net freshwater flux into the ocean ($m s^{-1}$) during the period 1950–2099 with the explained variances in the upper-left corners, compared with the Niño 3.4 index (red; 36-month low-pass filter). The historical and future periods are separated by the vertical grey lines in 2015

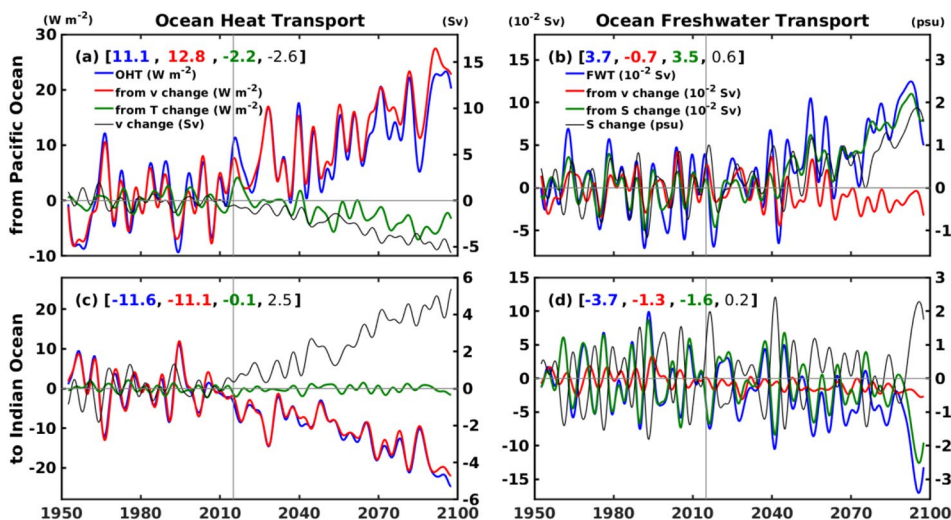
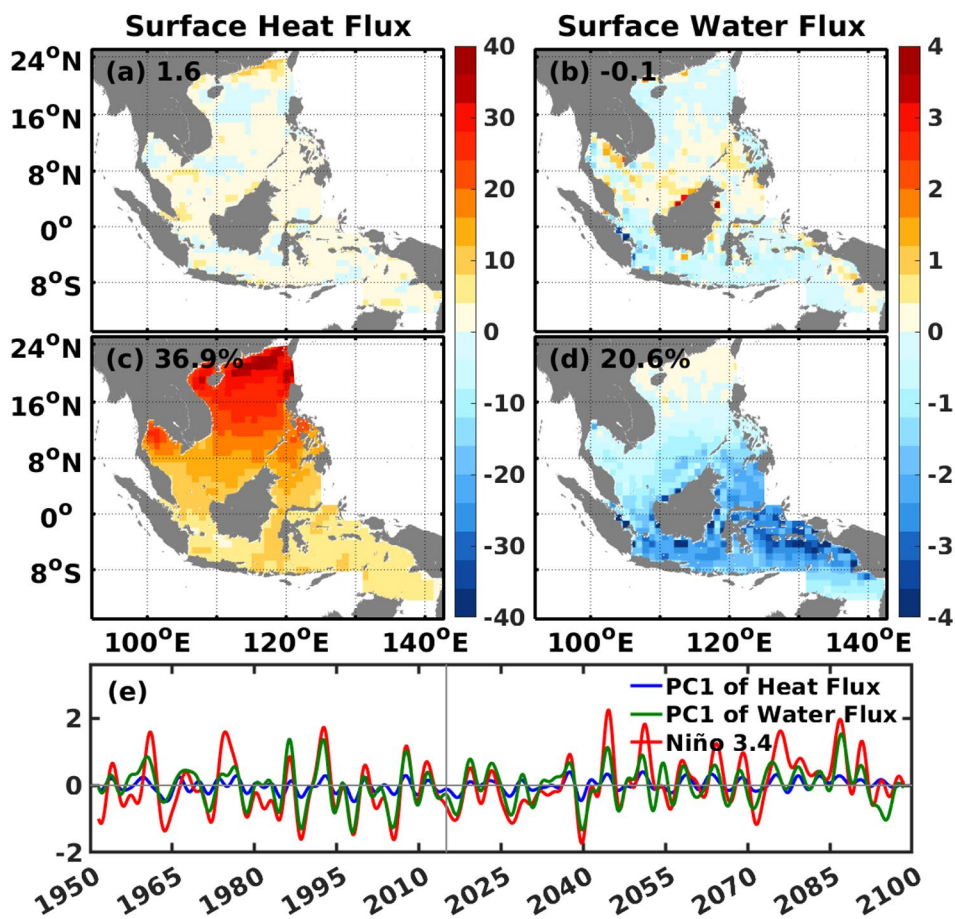


Fig. 6 (a) Ocean heat transport ($W m^{-2}$) and (b) freshwater transport ($10^{-2} Sv$) from the Pacific to the SEA. Total transports (relative to the historical mean; blue) are decomposed into the contributions from velocity change (red) and temperature change (or salinity change; green). The thin black lines in (a) and (b) show the volume transport changes (Sv) and salinity changes (psu) of inflow (from the Pacific to the SEA) and outflow (from the SEA to the Indian Ocean), respectively, which are both relative to their own historical means. (c-d) are

the same as (a-b) but for the transports flowing from the SEA into the Indian Ocean. The numbers in the corners indicate the time-mean changes of total transports (blue), the contributions from velocity change (red) and temperature/salinity change (green), and volume transport/salinity change (black) from historical (1950–2014) to future (2015–2099) periods. All the heat transports are divided by the SEA surface area. Historical and future periods are separated by vertical grey lines in 2015. A 5-year low-pass filter is applied to curves

In contrast, the contribution from the salinity change grows over time and has a larger standard deviation than that of the velocity, and becomes a more important factor to both the inflow and outflow FWTs (Fig. 6b and d). The contribution from salinity provides most of the time-mean changes of FWT with large explained variances (0.83 and 0.92) for both the inflow and outflow. As the same function of velocity change during OHT analysis, the time series of the salinity change (thin black lines in Fig. 6b and d) is also involved as a reference, which is defined as,

$$F_s = \frac{\iint_0^H (S_{mean} - S) dz dx}{\iint_0^H dz dx} \quad (7)$$

To be consistent with the definition of FWT, a positive F_s indicates smaller salinity than the regional mean. Therefore, it illustrates that the inflow-freshwater transport from the Pacific is enhanced with fresher water in the future, although the water volume transport is projected to decrease (Fig. 6b). The decreased outflow FWT is also caused by slightly freshened water (Fig. 6d). Unlike the situation of OHT, the outflow of FWT shows weak relation with the inflow (correlation -0.41 ; blue lines in Fig. 6b and d). As mentioned before, the reason for this is that the outflow FWT is not only influenced by the inflow FWT but also deeply affected by the SFF. However, the outflow OHT is dominated by the inflow OHT (6-month lag with correlation of -0.92), and the SHF is a response to the total OHT.

For the connection with ENSO, a significant impact of ENSO variability is found in the inflow volume transport (showing 7-month lead with correlation of -0.76 between Niño 3.4 index and inflow volume transport). Combined with the contribution from the atmosphere, we conclude that the physical processes of how ENSO variability influences the SEA region through ocean transports and air-sea fluxes as follows. During the El Niño (La Niña) events, a weaker (stronger) westward volume transport results in

smaller (larger) OHT to the SEA region, which could be caused by the weaker (stronger) easterly trade winds in the tropical Pacific, and further drives the SEA OHC change. Meanwhile, the eastward (westward) displaced warm pool results in lower (higher) upper-layer ocean temperature in the SEA region than during normal conditions. Then, the lower (higher) upper-layer ocean temperature during the El Niño (La Niña) events (1) promotes (hinders) the ocean obtaining additional heat from atmosphere, and (2) suppresses (enhances) rising air which leads to less (more) precipitation, reflected in the SHF and SFF, respectively. The FWC is firstly affected by the SFF, and then adjusted by the ocean divergent FWT. In the end, the modified OHC and FWC are manifested in the variabilities of TSSL and HSSL, respectively.

4.3 Ocean heat and freshwater transports through individual straits

Thanks to the high-resolution ocean model, transports through narrow straits around the SEA and local current changes are well resolved (Fig. 1). These 14 straits at different locations and cross-sectional areas provide different contributions to the OHC and FWC (Fig. 7), and we focus on the straits with top OHT and FWT. The OHTs through individual straits show that during the historical period Straits No. 2, 7 and 11 are the three largest positive contributors, while Straits No. 5, 10 and 12 provide the three largest negative OHTs (Fig. 7a). For the FWT, Straits No. 2 and 3 transport the most freshwater, and Straits No. 11 and 12 provide the top two negative FWTs (Fig. 7b). Considering the outflow OHT through Strait No. 10 is highly controlled by the inflow OHT through Strait No. 7 (Torres Strait), indicated by correlation of -0.68 and both of them show negligible linear trends (Fig. 7a), these two OHTs are excluded from our discussion. Therefore, the OHTs through Straits No. 2, 5, 11, 12 and FWTs through Straits No. 2, 3, 11, 12 are investigated specifically (Fig. 8). Geographically, Strait

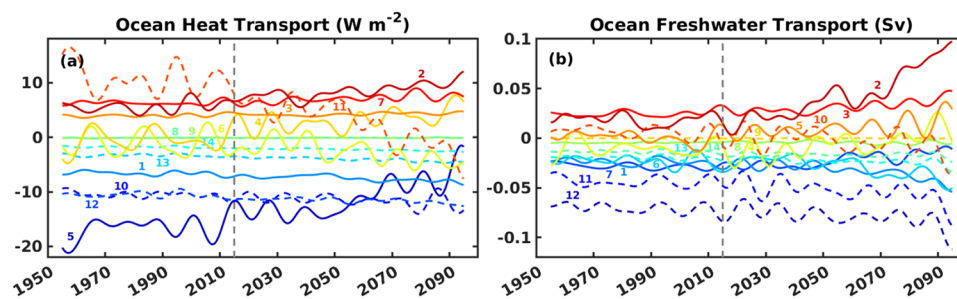


Fig. 7 (a) Time series (W m^{-2}) of ocean heat transport through individual straits (divided by the area of SEA region; numbers corresponding to straits in Fig. 1), in which the solid lines (Straits No. 1–7) indicate the transports on the Pacific side, and the dashed lines (Straits No. 8–14) show the transports on the Indian Ocean side. (b) is the same

as (a) but for freshwater transports. Positive values in (a) and (b) represent heating and freshening the SEA region, respectively. Historical and future periods are separated by vertical dashed lines in 2015. A 10-year low-pass filter is applied to all time series

No.2 (the Luzon Strait) is the entrance of the South China Sea Throughflow (SCSTF), where the Pacific water intrudes into the SCS. The SCSTF refers to the intrusion of the Kuroshio into the SCS through the Luzon Strait and outflow into the Indonesian seas through two major passages: the Karimata Strait and Mindoro–Sibutu Passage (Wei et al. 2016). Strait No.3 (Surigao Strait) is a narrow strait but provides one of the two significant secondary routes for both the ITF and the western boundary current of the Pacific northern tropical gyre (Hurlburt et al. 2011). Strait No.5 is one of the entrances of the ITF (close to the Lifamatola Strait), while Straits No. 11 (close to the Ombai Strait) and 12 (the Lombok Strait and nearby straits) are two exits of the ITF.

Based on the results of the transport decomposition, the trends and variability of the OHTs through all these four straits are mainly controlled by velocity change (Fig. 8a, c, e and g), which means the characteristic of the volume transport is very important for local TSSL in the SEA region. Specifically, the OHT through the Luzon Strait (Strait No.2) is enhanced during the future period caused by strengthened inflow volume transport (Fig. 8a). However, the OHT

through Strait No.5 also results in increasing OHC but with the reduced volume transport. The contrasting behavior is caused by the different long-term means of the difference between section temperature and regional mean temperature ($T - \bar{T}_{mean}$). The reduced volume transport through Strait No.5 (decreases 1.0 Sv over the future period based on Fig. 8c) contributes to the projected ITF weakening. Correspondingly, the ITF outflow through Strait No. 11 carries much of the reduction (2.6 Sv) contributing to the largest OHC decrease (Fig. 8e). As another exit of the ITF, Strait No. 12 shows much weaker OHT trend (0.1 Sv) than that through Strait No.11, but also contributes to the reduced ITF in the future (Fig. 8g).

In contrast, the trends and variability of the top four largest FWTs through the SEA ocean boundaries are mainly induced by salinity change, and volume change is the secondary contributor (except Strait No.11, where volume and salinity provide roughly equivalent contributions to FWT time-mean change; Fig. 8b, d, f and h). Specifically, the inflow from the Pacific to the SEA through the Luzon Strait (Strait No.2) becomes fresher, which results in more

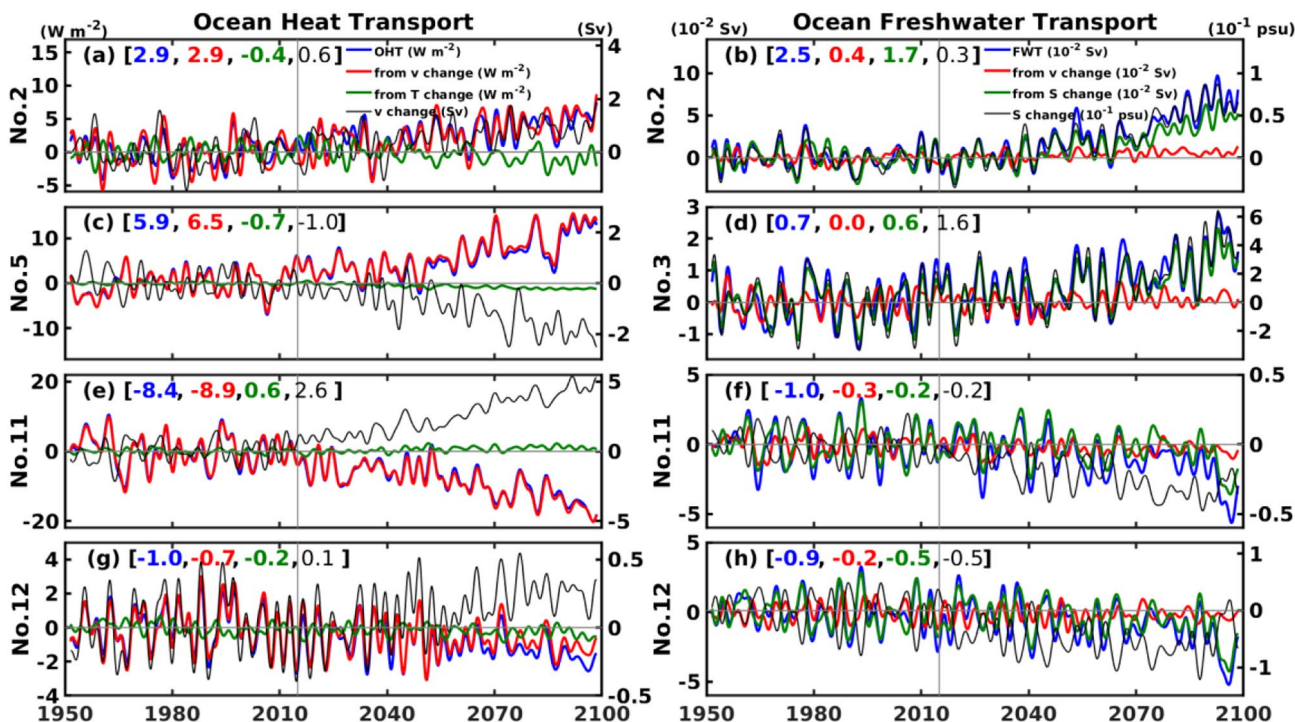


Fig. 8 (a) Ocean heat transport ($W m^{-2}$) and (b) freshwater transports (10^{-2} Sv) through Strait No.2. The total transports (relative to the historical mean; blue) are decomposed into the contributions from velocity change (red) and temperature change (or salinity change; green). Thin black lines in (a) and (b) show volume transport (Sv) and salinity (10^{-1} psu) changes, respectively. (c), (e) and (g) are the same as (a) but for the ocean heat and volume transport changes through Straits No.5, No.11 and No.12, respectively. (d), (f) and (h) are the same as (b) but for the ocean freshwater and salinity changes through Straits

No.3, No.11 and No.12, respectively. The numbers in the corners indicate the time-mean changes of total transports (blue), the contributions from velocity change (red) and temperature/salinity change (green), and volume transport/salinity change (black) from the historical (1950–2014) to future (2015–2099) periods. All the heat transports are divided by the SEA area to yield $W m^{-2}$. Historical and future periods are separated by vertical grey lines in 2015. A 5-year low-pass filter is applied to all time series

freshwater entering the SEA region. The Surigao Strait (Strait No.3) is a narrow and shallow strait but contributes quite large amounts of freshwater, which increases mainly due to the decreased salinity in the future. For the Straits No. 11 and 12, the FWTs are both projected to result in smaller FWC in the SEA. The ocean freshening in the Pacific and the SEA is reflected in the projected HSSL rising in the future, leading to 2.2 cm regional mean sea level rise in the SEA region at the end of 21st century (Fig. 2c).

By comparing all the individual OHTs on the Pacific side (solid lines in Fig. 7a), the OHT through Strait No. 5 shows the most obvious positive trend, and it is the largest contributor to the increasing trend of the total inflow OHT. The OHT through Strait No.5 always cools the SEA region (Fig. 7a) and the volume transport reduction of the generally cold (relative to the regional mean) inflow through Strait No.5 contributes most of the OHC rise in the scenario. Therefore, caused by the spatial-nonuniform volume transport change (i.e., much more pronounced volume transport reduction through Strait No.5 than the other inflow transport), the total inflow OHT from the Pacific turns from cooling to heating the SEA region in the scenario (yellow dashed line in Fig. 4a). While, based on the individual FWTs on the Pacific side (solid lines in Fig. 7b), the change of the total inflow FWT from salinizing to freshening the SEA region (yellow dashed line in Fig. 4c) is mainly induced by the freshening inflow transport through Strait No.2.

4.4 Pathways changing in the western Pacific and SEA region

In addition, we find that the trend and variability of the volume transport through the Luzon Strait (Strait No.2) is closely connected with the volume transport change of the ITF. The volume transport through Strait No. 4 (the channel between the Mindanao Island and the Sulawesi's Minahasa Peninsula, which is the dominant entrance of the ITF) shows an opposite linear trend and inverse variability (correlation of -0.81) against the transport through Strait No.2, and it exhibits synchronous variability to that in Strait No.5 (correlation of 0.74; Fig. S2).

The regional circulation change is likely to be induced by signals from its upstream. To examine the potential mechanism, the meridional variation of the volume transport from the Pacific to the SEA region is quantified, which is defined as the latitude change of the averaged "center of zonal water velocity" in the western Pacific near the Philippines islands (following the measurement-based method in Yang et al. 2020):

$$P = \frac{\int (u_{min} - u) \cdot lat}{\int (u_{min} - u)}, \quad (8)$$

where P is the averaged latitude of zonal water velocity, lat is the latitude ranging from 0° to 24°N covering both Straits No.2 and 4, u_{min} is the minimum westward zonal water velocity, and u is the averaged zonal water velocity corresponding to lat . Both u_{max} and u are zonally averaged within 129° - 132°E (between the two red lines in Fig. 1). Before the calculation, the eastward velocities are excluded, so only the westward velocities are counted, and a larger weight is given to the latitude with larger westward velocity when averaging.

The latitude changes of the westward velocity center are calculated for the surface (0-200 m) and subsurface (200-4000 m) layers, respectively (Fig. 9). The linear regression (dashed lines in Fig. 9) indicates that the latitude of the averaged center of zonal velocity within surface layer moves northward during the future period (0.64° per century). Similarly, the subsurface velocity center also moves northward but with weaker trend (0.15° per century). The near-surface change should be related to the projected northward shift of the North Equatorial Current bifurcation latitude connected with surface wind stress change (e.g., Duan et al. 2017; Yang et al. 2020). The northward shifting causes that part of the volume transport previously flowing through Straits No. 4 and 5 is progressively entering the SCS through Strait No. 2 in the future. Consequently, the outflowing volume transport through Strait No. 11 is reduced responding to the decreasing volume transport through Straits No.4 and 5. In the future, as larger volume is transported through Strait No. 2 into the SCS, the anticlockwise circulation in the SCS enhances, which imprints on the DSL change (Fig. 2a). The volume transport changes along the pathways of the ITF and SCSTF are clearly illustrated by comparing the pattern from the historical period of depth-averaged current with its projected changes (Fig. 10), which are consistent with the results of CMIP5 multi-model ensemble mean (Hu et al. 2015). These changes occur mainly in the surface layer (0-200 m; Fig. 10b), although the subsurface (200-4000 m) also shows slightly ITF weakening (Fig. 10d).

5 Summary and discussion

Based on the output of the coupled model MPI-ESM-ER with its high-resolution ocean component, we investigate the sea-level trends and variability in the SEA region during the historical and a strong global warming scenario for the future (SSP5-8.5). Our results reveal that (1) the SEA sea level is deeply influenced by ENSO variability. Specifically, ENSO affects TSSL mainly through ocean transport, while it impacts HSSL mainly through air-sea fluxes. (2) Fluxes from the air-sea interface and transports through ocean straits provide roughly equivalent contributions to

Fig. 9 Time series (red) of the latitude of the westward velocity center (Eq. 5) averaged between the two red lines in Fig. 1 within top 200 m after 5-year low-pass filter. Dashed lines represent the linear trends of the historical and future periods, respectively. The blue lines are the same as the red lines, but for velocity averaged within 200–4000 m. The linear trends of the velocity averaged within top 200 m during the historical and future periods are -0.06° per century and 0.64° per century, respectively. The linear trends of the velocity averaged within 200–4000 m during the historical and future periods are -0.16° per century and 0.15° per century, respectively

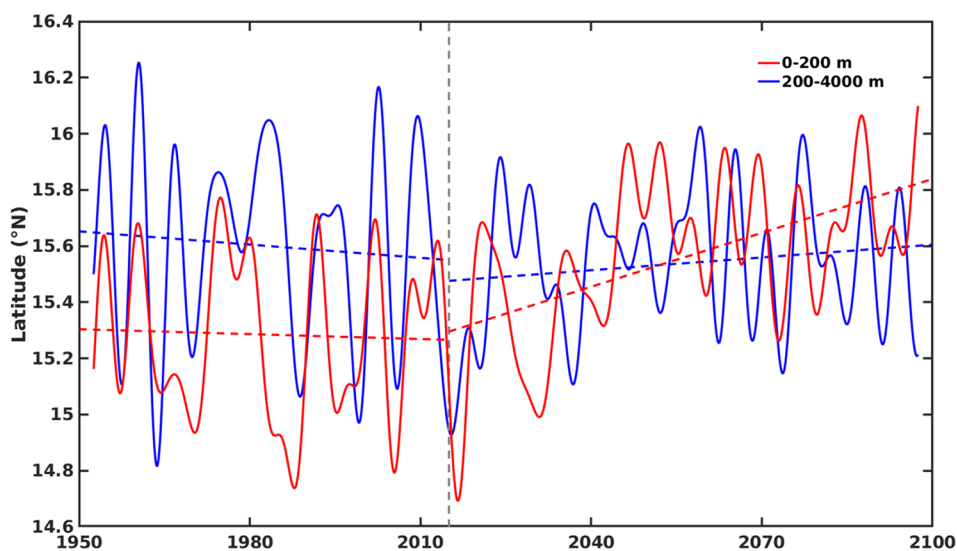
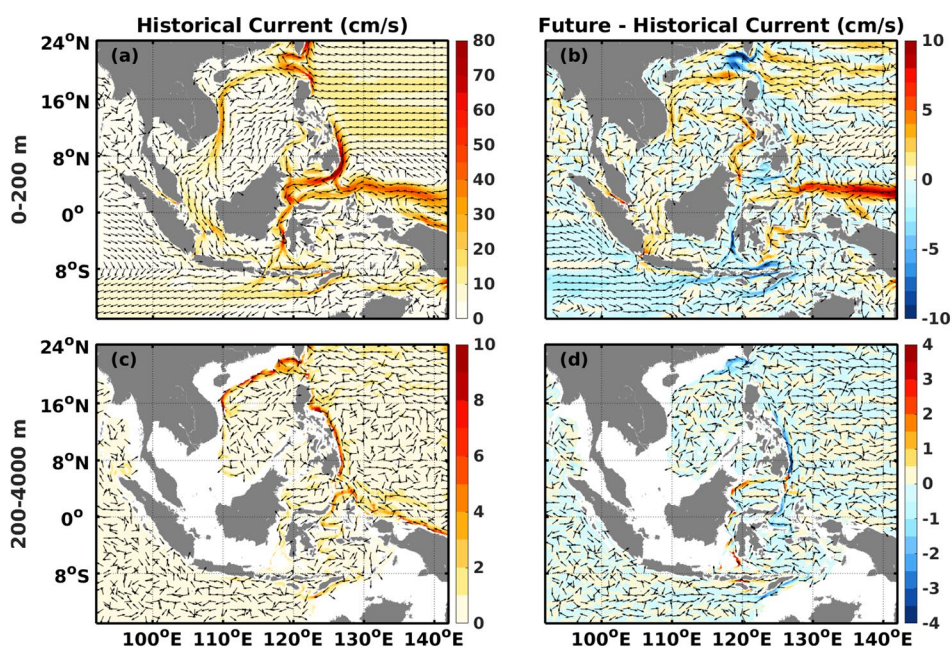


Fig. 10 Mean ocean current (cm s^{-1}) (a) averaged over the top 200-m during 1995–2014, and (b) projected changes during the 2080–2099 relative to 1995–2014. (c-d) are the same as (a-b) but averaged between 200–4000 m depth. The color shading indicates current speed, and the arrows only show current directions



both OHC and FWC growing. (3) Ocean transport impacts SEA OHC mainly through the reduced volume transport, but affects FWC by freshening water. (4) The dominant zonal surface current from the Pacific to the SEA region is found to move northward, resulting in a weakening ITF and a strengthening SCSTF.

Beyond our current conclusions, there are several interesting topics worth discussing. ENSO variability can lead to roughly 9 cm sea-level fluctuation (peak to peak) on the continental shelves of the SEA region. According to observation and reanalysis data, some studies suggest more frequent extreme El Niño (e.g., Cai et al. 2014; Wang et al. 2017) and La Niña (e.g., Cai et al. 2015; Marjani et al. 2019) events to

occur under greenhouse warming, which according to our results should result in more extreme sea level events in the SEA region on interannual time scale. Based on MPI-ESM-ER, we find both extreme El Niño and extreme La Niña (defined as the events when the Niño 3.4 index is larger than 1.5°C and lower than -1.5°C respectively) are becoming more frequent over the future period. However, there is still no clear consensus about the projected ENSO variability change in the future, largely because of the uncertainty among different climate models (e.g., Beobide-Arsuaga et al. 2021). In addition, another study finds that the pathway changes of the currents within the SEA region can in turn modify ENSO variability by affecting the surface forcing

(Tozuka et al. 2015). We also find that ENSO variability leads by 4-month (6-month) the OHC (FWC) variability in the SEA region, which facilitates a prediction potential of the sea-level variability in the SEA from ENSO.

Besides, the projected increasing OHT from the Pacific to the SEA region is mainly caused by the reduced volume transport. However, pronounced ocean salinity reduction for the inflow from the Pacific provides a larger contribution than the reduced volume transport to the FWT changes. This difference is caused by the fact that the SEA region and the western Pacific warm similarly in the future, while showing distinguished salinity characteristics. Previously, Cravatte et al. (2009) observed significant freshening in the western Pacific Warm Pool during 1955–2003, which is related to the enhancement of the hydrological cycle. Based on coral oxygen isotopic time series, Linsley et al. (2006) found the fresher western Pacific Warm Pool is influenced by the South Pacific Convergence Zone expansion. This freshening might continue in the future due to enhanced precipitation in the Pacific (e.g., Langenbrunner et al. 2015; Wang et al. 2020), which means the HSSL in the SEA region will keep rising under climate change.

Locally, the interaction between the ITF and SCSTF was discussed in connection with seasonal and interannual time scales (e.g., Gordon et al. 2012; Wei et al. 2016). In this study, we demonstrate that such changes also take place under climate change conditions. Although the northward movement in the future period is mainly reflected in the surface layer, the current center in the subsurface also indicates a northward trend, reversing a southward trend during the historical period. Therefore, the changes in the subsurface layer could also be a matter of concern, which cannot be simply explained by surface wind stress (Wang et al. 2015; Chen et al. 2019). Some studies discovered a baroclinic response (i.e., spin up circulation in the upper ocean and spin down at the subsurface) in the Pacific under climate change, which is caused by the projected stronger warming in the upper ocean compared to that in the deeper ocean, leading to strengthened stratification and hindered vertical mixing of heat (e.g., Zhang et al. 2014; Wang et al. 2015; Chen et al. 2019). The same dynamical processes could also influence the OHC and FWC and thus sea level in the SEA region.

The SDSL and its components in the SEA region are closely connected with global warming, indicating accelerating trends under rapid and unconstrained energy consuming scenario (SSP5-8.5) while its variability is linked to ENSO. The conclusions drawn in this work contribute to a better understanding of projected sea-level trends and variability in the SEA region, which is critically needed for adaptation measures in response to future climate changes.

Supplementary Information The online version contains supplementary material available at <https://doi.org/10.1007/s00382-023-06960-y>.

Acknowledgements We thank Dian Putrasahan for conducting the MPI-ESM-ER experiments and providing the data. The data computation and visualization are supported by the Deutschen Klimarechenzentrum (DKRZ). The work contributes to the Centrum für Erdsystemforschung und Nachhaltigkeit (CEN) of Universität Hamburg.

Author contributions YJ and AK contributed to the study conception and design. Methodology was supported by AK. Data analysis and figures visualization were performed by YJ. The first draft of the manuscript was written by YJ and all authors commented on previous versions of the manuscript. All authors read and approved the final manuscript.

Funding This work was funded by the Deutsche Forschungsgemeinschaft (DFG) as a part of the Causes of Decadal to Centennial Regional Sea Level Variations (DECVAR-2), Special Priority Program (SPP-1889) Regional Sea Level Change & Society ‘SeaLevel’.

Data Availability The altimetry products of the Archiving, Validation and Interpretation of Satellite Oceanographic (AVISO) are from https://data.marine.copernicus.eu/product/SEALEVEL_GLO_PHY_L4_MY_008_047/description. The MPI-ESM-ER data are available at the World Data Centre for Climate hosted at DKRZ under <https://www.wdc-climate.de/ui/q?query=PRIMAVERA&page=0&rows=15>.

Declarations

Competing interests The authors declare no competing interests.

References

- Ablain M et al (2019) Uncertainty in satellite estimates of global mean sea-level changes, trend and acceleration. *Earth Syst Sci Data* 11(3):1189–1202. <https://doi.org/10.5194/essd-11-1189-2019>
- Beobide-Arsuaga G, Bayr T, Reintges A, Latif M (2021) Uncertainty of ENSO-amplitude projections in CMIP5 and CMIP6 models. *Clim Dyn* 56(11):3875–3888. <https://doi.org/10.1007/s00382-021-05673-4>
- Cai W et al (2014) Increasing frequency of extreme El Niño events due to greenhouse warming. *Nat Clim Change* 4(2):111–116. <https://doi.org/10.1038/nclimate2100>
- Cai W et al (2015) Increased frequency of extreme La Niña events under greenhouse warming. *Nat Clim Change* 5(2):132–137. <https://doi.org/10.1038/nclimate2492>
- Cazenave A, Cozannet GL (2014) Sea level rise and its coastal impacts. *Earths Future* 2(2):15–34. <https://doi.org/10.1002/2013EF000188>
- Chen C, Wang G, Xie SP, Liu W (2019) Why does global warming weaken the Gulf Stream but intensify the Kuroshio? *J Clim* 32(21):7437–7451. <https://doi.org/10.1175/JCLI-D-18-0895.1>
- Cravatte S, Delcroix T, Zhang D, McPhaden M, Leloup J (2009) Observed freshening and warming of the western Pacific warm pool. *Clim Dyn* 33(4):565–589. <https://doi.org/10.1007/s00382-009-0526-7>
- Duan J, Chen Z, Wu L (2017) Projected changes of the low-latitude north-western Pacific wind-driven circulation under global warming. *Geophys Res Lett* 44(10):4976–4984. <https://doi.org/10.1002/2017GL073355>

- Fox-Kemper B et al (2021) Ocean, Cryosphere and Sea Level Change. In: Masson-Delmotte V et al (eds) Climate Change 2021: the physical science basis. Contribution of Working Group I to the Sixth Assessment Report of the Intergovernmental Panel on Climate Change. Cambridge University Press, Cambridge, United Kingdom and New York, NY, USA, pp 1211–1362. <https://doi.org/10.1017/9781009157896.011>.
- Frankcombe LM, McGregor S, England MH (2015) Robustness of the modes of Indo-Pacific sea level variability. *Clim Dyn* 45:1281–1298. <https://doi.org/10.1007/s00382-014-2377-0>
- Gordon AL et al (2010) The Indonesian throughflow during 2004–2006 as observed by the INSTANT program. *Dyn Atmos Oceans* 50(2):115–128. <https://doi.org/10.1016/j.dynatmoce.2009.12.002>
- Gordon AL, Huber BA, Metzger EJ, Susanto RD, Hurlburt HE, Adi TR (2012) South China Sea throughflow impact on the Indonesian throughflow. *Geophys Res Lett* 39(11). <https://doi.org/10.1029/2012GL052021>
- Gregory JM et al (2019) Concepts and terminology for sea level: Mean, variability and change, both local and global. *Surv Geophys* 40:1251–1289. <https://doi.org/10.1007/s10712-019-09525-z>
- Gupta AS, Jourdain NC, Brown JN, Monselesan D (2013) Climate Drift in the CMIP5 models. *J Clim* 26(21):8597–8615. <https://doi.org/10.1175/JCLI-D-12-00521.1>
- Gupta AS, McGregor S, Van Sebille E, Ganachaud A, Brown JN, Santoso A (2016) Future changes to the Indonesian Throughflow and Pacific circulation: the differing role of wind and deep circulation changes. *Geophys Res Lett* 43(4):1669–1678. <https://doi.org/10.1002/2016GL067757>
- Gupta AS, Stellema A, Pontes GM, Taschetto AS, Vergés A, Rossi V (2021) Future changes to the upper ocean western boundary currents across two generations of climate models. *Sci Rep* 11(1):1–12. <https://doi.org/10.1038/s41598-021-88934-w>
- Gutjahr O, Putrasahan D, Lohmann K, Jungclauss JH, Storch JS, Brüggemann N, Haak H, Stössel A (2019) Max planck institute earth system model (MPI-ESM1. 2) for the high-resolution model intercomparison project (HighResMIP). *Geosci Model Dev* 12(7):3241–3281. <https://doi.org/10.5194/gmd-12-3241-2019>
- Haarsma RJ et al (2016) High Resolution Model Intercomparison Project (HighResMIP v1.0) for CMIP6. *Geosci Model Dev* 9(11):4185–4208. <https://doi.org/10.5194/gmd-9-4185-2016>
- Hu D et al (2015) Pacific western boundary currents and their roles in climate. *Nature* 522(7556):299–308. <https://doi.org/10.1038/nature14504>
- Hurlburt HE, Metzger EJ, Sprintall J, Riedlinger SN, Arnone RA, Shindoda T, Xu X (2011) Circulation in the Philippine Archipelago simulated by 1/12 and 1/25 global HYCOM and EAS NCOM. *Oceanography* 24(1):28–47. <https://www.jstor.org/stable/24861238>
- Jin Y, Zhang X, Church JA, Bao X (2021) Projected Sea Level Changes in the marginal Seas near China based on Dynamical Downscaling. *J Clim* 34(17):7037–7055. <https://doi.org/10.1175/JCLI-D-20-0796.1>
- Köhl A, Serra N (2014) Causes of decadal changes of the freshwater content in the Arctic Ocean. *J Clim* 27(9):3461–3475. <https://doi.org/10.1175/JCLI-D-13-00389.1>
- Landerer FW, Jungclauss JH, Marotzke J (2007) Ocean bottom pressure changes lead to a decreasing length-of-day in a warming climate. *Geophys Res Lett* 34(6). <https://doi.org/10.1029/2006GL029106>
- Langenbrunner B, Neelin JD, Lintner BR, Anderson BT (2015) Patterns of precipitation change and climatological uncertainty among CMIP5 models, with a focus on the midlatitude Pacific storm track. *J Clim* 28(19):7857–7872. <https://doi.org/10.1175/JCLI-D-14-00800.1>
- Lee T, Fukumori I, Tang B (2004) Temperature advection: internal versus external processes. *J Phys Oceanogr* 34(8):1936–1944. [https://doi.org/10.1175/1520-0485\(2004\)034%3C1936:TAIVEP%3E2.0.CO;2](https://doi.org/10.1175/1520-0485(2004)034%3C1936:TAIVEP%3E2.0.CO;2)
- Lee T, Awaji T, Balmaseda M et al (2010) Consistency and fidelity of Indonesian-throughflow total volume transport estimated by 14 ocean data assimilation products. *Dyn Atmos Oceans* 50(2):201–223. <https://doi.org/10.1016/j.dynatmoce.2009.12.004>
- Linsley BK, Kaplan A, Gouriou Y, Salinger J, deMenocal PB, Wellington GM, Howe SS (2006) Tracking the extent of the South Pacific Convergence Zone since the early 1600s. *Geochem Geophys Geosystems* 7(5). <https://doi.org/10.1029/2005GC001115>
- Liu Q, Feng M, Wang D (2011) ENSO-induced interannual variability in the southeastern South China Sea. *J Oceanogr* 67:127–133. <https://doi.org/10.1007/s10872-011-0002-y>
- Lyu K, Zhang X, Church JA (2020) Regional dynamic sea level simulated in the CMIP5 and CMIP6 models: mean biases, future projections, and their linkages. *J Clim* 33(15):6377–6398. <https://doi.org/10.1175/JCLI-D-19-1029.1>
- Marjani S, Alizadeh-Choobari O, Irannejad P (2019) Frequency of extreme El Niño and La Niña events under global warming. *Clim Dyn* 53(9):5799–5813. <https://doi.org/10.1007/s00382-019-04902-1>
- Mauritsen T et al (2019) Developments in the MPI-M Earth System Model version 1.2 (MPI-ESM1. 2) and its response to increasing CO₂. *J Adv Model Earth Syst* 11(4):998–1038. <https://doi.org/10.1029/2018MS001400>
- Müller WA et al (2018) A higher-resolution version of the Max Planck Institute Earth System Model (MPI-ESM1. 2-HR). *J Adv Model Earth Syst* 10(7):1383–1413
- Rabe B et al (2011) An assessment of Arctic Ocean freshwater content changes from the 1990s to the 2006–2008 period. *Deep Sea Res Part I. Oceanogr Res Pap* 58(2):173–185. <https://doi.org/10.1016/j.dsr.2010.12.002>
- Rayner NA, Parker DE, Horton EB, Folland CK, Alexander LV, Rowell DP, Kent EC, Kaplan A (2003) Global analyses of sea surface temperature, sea ice, and night marine air temperature since the late nineteenth century. *J Geophys Res Atmospheres* 108(D14):4407. <https://doi.org/10.1029/2002JD002670>
- Rong Z, Liu Y, Zong H, Cheng Y (2007) Interannual sea level variability in the South China Sea and its response to ENSO. *Glob Planet Change* 55(4):257–272. <https://doi.org/10.1016/j.gloplacha.2006.08.001>
- Shilimkar V, Abe H, Roxy MK, Tanimoto Y (2022) Projected future changes in the contribution of Indo-Pacific sea surface height variability to the Indonesian throughflow. *J Oceanogr* 78(5):337–352. <https://doi.org/10.1007/s10872-022-00641-w>
- Slangen ABA et al (2014) Projecting twenty-first century regional sea-level changes. *Clim Change* 124:317–332. <https://doi.org/10.1007/s10584-014-1080-9>
- Sprintall J, Wijffels SE, Molcard R, Jaya I (2009) Direct estimates of the Indonesian throughflow entering the Indian Ocean: 2004–2006. *J Geophys Res Oceans* 114(C7). <https://doi.org/10.1029/2008JC005257>
- Strassburg MW, Hamlington BD, Leben RR, Manurung P, Lumban Gaol J, Nababan B, Vignudelli S, Kim KY (2015) Sea level trends in southeast Asian seas. *Clim Past* 11(5):743–750. <https://doi.org/10.5194/cp-11-743-2015>
- Sun S, Thompson AF (2020) Centennial changes in the Indonesian throughflow connected to the Atlantic meridional overturning circulation: the ocean’s transient conveyor belt. *Geophys Res Lett* 47(21). <https://doi.org/10.1029/2020GL090615>
- Thompson PR, Piecuch CG, Merrifield MA, McCreary JP, Firing E (2016) Forcing of recent decadal variability in the Equatorial and North Indian Ocean. *J Geophys Res Oceans* 121(9):6762–6778. <https://doi.org/10.1002/2016JC012132>
- Tozuka T, Tangdong Q, Yamagata T (2015) Impacts of South China Sea throughflow on the mean state and El Niño/Southern Oscillation

- as revealed by a coupled GCM. *J Oceanogr* 71(1):105–114. <https://doi.org/10.1007/s10872-014-0265-1>
- Trenberth KE (1997) The definition of El Niño. *Bull Am Meteorol Soc* 78(12):2771–2778. [https://doi.org/10.1175/1520-0477\(1997\)078%3C2771:TDOENO%3E2.0.CO;2](https://doi.org/10.1175/1520-0477(1997)078%3C2771:TDOENO%3E2.0.CO;2)
- Wang G, Xie SP, Huang RX, Chen C (2015) Robust warming pattern of global subtropical oceans and its mechanism. *J Clim* 28:8574–8584. <https://doi.org/10.1175/JCLI-D-14-00809.1>
- Wang G, Cai W, Gan B, Wu L, Santosa A, Lin X, Chen Z, McPhaden MJ (2017) Continued increase of extreme El Niño frequency long after 1.5 C warming stabilization. *Nat Clim Change* 7(8):568–572. <https://doi.org/10.1038/nclimate3351>
- Wang B, Jin C, Liu J (2020) Understanding future change of global monsoons projected by CMIP6 models. *J Clim* 33(15):6471–6489. <https://doi.org/10.1175/JCLI-D-19-0993.1>
- Wei J, Li MT, Malanotte-Rizzoli P, Gordon AL, Wang DX (2016) Opposite variability of Indonesian throughflow and South China Sea throughflow in the Sulawesi Sea. *J Phys Oceanogr* 46(10):3165–3180. <https://doi.org/10.1175/JPO-D-16-0132.1>
- Wetzel FT, Beissmann H, Penn DJ, Jetz W (2013) Vulnerability of terrestrial island vertebrates to projected sea-level rise. *Glob Change Biol* 19(7):2058–2070. <https://doi.org/10.1111/gcb.12185>
- Wickramage C, Köhl A, Jungclaus J, Stammer D (2023) Sensitivity of MPI-ESM Sea Level Projections to its ocean spatial resolution. *J Clim* 1–56. <https://doi.org/10.1175/JCLI-D-22-0418.1>
- Wieners KH, Giorgetta M, Jungclaus J, Reick C, Esch M, Bittner M, Roeckner E (2019) MPI-M MPI-ESM1.2-LR model output prepared for CMIP6 ScenarioMIP ssp126. <https://doi.org/10.22033/ESGF/CMIP6.6690>. Earth System Grid Federation
- Wu Q, Zhang X, Church JA, Hu J (2017) Variability and change of sea level and its components in the Indo-Pacific region during the altimetry era. *J Geophys Res Oceans* 122(3):1862–1881. <https://doi.org/10.1002/2016JC012345>
- Yang H, Lohmann G, Krebs-Kanzow U, Ionita M, Shi X, Sidorenko D, Gong X, Chen X, Gowan EJ (2020) Poleward shift of the major ocean gyres detected in a warming climate. *Geophys Res Lett* 47(5). <https://doi.org/10.1029/2019GL085868>
- Zhang X, Church JA (2012) Sea level trends, interannual and decadal variability in the Pacific Ocean. *Geophys Res Lett* 39(21). <https://doi.org/10.1029/2012GL053240>
- Zhang X, McPhaden MJ (2010) Surface layer heat balance in the eastern equatorial Pacific Ocean on interannual time scales: influence of local versus remote wind forcing. *J Clim* 23(16):4375–4394. <https://doi.org/10.1175/2010JCLI13469.1>
- Zhang X, Church JA, Platten SM, Monselesan D (2014) Projection of subtropical gyre circulation and associated sea level changes in the Pacific based on CMIP3 climate models. *Clim Dyn* 43:131–144. <https://doi.org/10.1007/s00382-013-1902-x>

Publisher's Note Springer Nature remains neutral with regard to jurisdictional claims in published maps and institutional affiliations.

Springer Nature or its licensor (e.g. a society or other partner) holds exclusive rights to this article under a publishing agreement with the author(s) or other rightsholder(s); author self-archiving of the accepted manuscript version of this article is solely governed by the terms of such publishing agreement and applicable law.